Chemical Science

ROYAL SOCIETY OF CHEMISTRY

EDGE ARTICLE

View Article Online
View Journal | View Issue

Check for updates

Cite this: *Chem. Sci.*, 2023, **14**, 323

All publication charges for this article have been paid for by the Royal Society of Chemistry

Received 23rd November 2022
Accepted 5th December 2022

DOI: 10.1039/d2sc06445f

rsc.li/chemical-science

Open Access Article. Published on 12 December 2022. Downloaded on 12/5/2025 11:51:35 PM.
This article is licensed under a Creative Commons Attribution-NonCommercial 3.0 Unported Licence.

Unveiling upsurge of photogenerated ROS: control of intersystem crossing through tuning aggregation patterns†

Junjun Wang,‡[a] Hao Li,‡[b] Yicai Zhu,[a] Mingdi Yang,[c] Jing Huang,[c] Xiaojiao Zhu,[a] Zhi-Peng Yu,*[a] Zhou Lu [b] and Hongping Zhou *[a]

Photo-induced reactive oxygen species (ROS) generation by organic photosensitizers (PSs), which show potential in significant fields such as photodynamic therapy (PDT), are highly dependent on the formation of the excited triplet state through intersystem crossing (ISC). The current research on ISC of organic PSs generally focuses on molecular structure optimization. In this manuscript, the influence of aggregation patterns on ISC was investigated by constructing homologous monomers (S-TPA-PI and L-TPA-PI) and their homologous dimers (S-2TPA-2PI and L-2TPA-2PI). In contrast to *J*-aggregated S-TPA-PI, S-2TPA-2PI-aggregate forming "end-to-end" stacking through π–π interaction could generate ROS more efficiently, due to a prolonged exciton lifetime and enhanced ISC rate constant (k_{ISC}), which were revealed by femtosecond transient absorption spectroscopy and theoretical calculations. This finding was further validated by the regulation of aggregation patterns induced by host–guest interaction. Moreover, S-2TPA-2PI could target mitochondria and achieve rapid mitophagy to cause more significant cancer cell suppression. Overall, the delicate supramolecular dimerization tactics not only revealed the structure–property relationship of organic PSs but also shed light on the development of a universal strategy in future PDT and photocatalysis fields.

Introduction

Organic photosensitizers (PSs) could convert substrates (oxygen, water, *etc.*)[1,2] into reactive oxygen species (ROS) upon illumination, providing advantages in the photon-triggered therapeutic strategy[3–5] and photocatalysis.[6] During this process, a critical step is that electrons in the excited singlet state (S_1) will undergo a fast spin-flip, achieving an excited triplet state (T_1) through intersystem crossing (ISC).[7] It is reported that the ISC rate is crucial to the depopulation of the S_1.[8] To promote ISC progress and realize efficient ROS release, various strategies are used to manipulate the energy gap (ΔE_{ST}) between S_1 and T_1, such as the heavy atom effect, a bent molecular skeleton,[9] strong donor–acceptor (D–A), and/or the extended conjugate length.[10–12] Apart from the molecular structure, the aggregation pattern of a PS was recognized as the more important issue affecting ROS generation.[13–16] Tang *et al.* found that a PS improved ROS production in aggregation due to the enhanced spin-orbital coupling (SOC) to promote ISC, which further confirmed the importance of intermolecular forces in ROS production.[17] Therefore, the intermolecular forces affected by different aggregation patterns, stacking compactness, the strength of intermolecular forces, and so on need to be considered.

As is well known, the complex aggregation mode of organic materials affects the excited state process, resulting in differentiated photochemical and photophysical properties.[18–21] For example, the well-known AIE characteristic tends to occur in *J*-aggregates or *H*-aggregates.[22] Except for basic optical properties such as fluorescence, the ROS release was more complicated owing to the involved electron- or energy-transfer process between PSs and the substrate (*e.g.* O_2, H_2O, *etc*). Current studies mainly focus on the differences in ROS between the aggregated state (AS) and the monodisperse states (MS) of the PS.[23–25] However, there is no corresponding research to further discuss the underlying mechanism between different ASs. Reasonable molecular models for the above studies were highly desired, which can construct different aggregation

[a]*School of Chemistry and Chemical Engineering, Institute of Physical Science and Information Technology, Anhui University and Key Laboratory of Functional Inorganic Materials Chemistry of Anhui Province, Anhui Province Key Laboratory of Chemistry for Inorganic/Organic Hybrid Functionalized Materials, Key Laboratory of Structure and Functional Regulation of Hybrid Materials (Anhui University) Ministry of Education, Hefei, 230601, P.R. China. E-mail: zhpzhp@263.net; zpyu@ahu.edu.cn*

[b]*Anhui Province Key Laboratory of Optoelectronic Material Science and Technology School of Physics and Electronic Information, Anhui Normal University, Wuhu 241002, China*

[c]*School of Materials and Chemical Engineering, Anhui Jianzhu University, Hefei 230601, P. R. China*

† Electronic supplementary information (ESI) available: The results of ^{1}H-NMR, ^{13}C-NMR, ESI-MS, DLS, TEM, UV-vis, fluorescence, fs-TA, theoretical calculation and CLSM of nano-PSs. CCDC 2133231–2141363. For ESI and crystallographic data in CIF or other electronic format see DOI: https://doi.org/10.1039/d2sc06445f

‡ J. W. and H. L. contributed equally.

© 2023 The Author(s). Published by the Royal Society of Chemistry

Open Access Article. Published on 12 December 2022. Downloaded on 12/5/2025 11:51:35 PM. This article is licensed under a Creative Commons Attribution-NonCommercial 3.0 Unported Licence.

patterns without interference from the changed molecular skeleton.

Dimeric molecular models with homologous chromophores are a valuable measure to modulate aggregation patterns. Additionally, compared to monomers, dimeric molecules with homologous chromophores displayed unique photophysical properties due to the intramolecular and intermolecular interactions.[26–30] K. George Thomas believed that the folding of the dimers made the chromophore molecules accumulate, which would further limit the molecular torsion and lead to a longer lifetime.[31] Moreover, our previous studies have also presented the promise of dimeric molecules in ROS generation and PDT.[32–34] Therefore, the dimeric molecular models were more conducive to exploring the effect of ROS generation among different aggregation patterns.

In this work, two monomeric molecules (S-TPA-PI and L-TPA-PI) were purposefully prepared with a homologous D–π–A core *via* triphenylamine (TPA) as the D, pyridine salt (PI) as the A and the olefinic bond as the π-bridge, which were connected with the flexible oligo-ethylene glycol to form the corresponding dimers (S-2TPA-2PI and L-2TPA-2PI). Based on the propeller-type TPA, they all displayed excellent AIE properties with the formation of similar nanoaggregates. Notably, in aggregation, the two dimers presented more efficient ROS generation to suppress cancer cells, while the two monomers had a negligible ROS yield. The single crystal structure analysis and femtosecond (fs) transient absorption spectroscopy unveiled that the "end-to-end" stacking of dimer-aggregates would achieve a longer excited singlet state lifetime (~500 folds) than the monomer-aggregate, allowing the acceleration of ISC for the generation of ROS. Furthermore, time-dependent density functional theory verified that a dimer with "end-to-end" stacking enhanced the spin–orbit coupling to achieve efficient ISC for ROS generation. In addition, cucurbit[8]uril was utilized to change the stacking pattern of S-TPA-PI for activating ROS, which further certified that the aggregation pattern affected ROS production. These dimeric molecular models would offer valuable insights to explore structure-engineering modulations for the promotion of ROS in nano-PSs (Scheme 1).

Results and discussion

Synthesis and characterization

As shown in Fig. 1 and Scheme S1 (ESI†), the four compounds were conveniently synthesized by two-step routes. The intermediates M1, M2, M3, and M4 were obtained from 4-methylpyridine through a substitution reaction. Then, M1, M2, M3, and M4 reacted with 4-(di-phenylamino) benzaldehyde through Knoevenagel condensation to yield the target molecules, respectively. Their chemical structures were fully characterized by ^{1}H-NMR, ^{13}C-NMR, and ESI-MS (Fig. S1–12†).

Photophysical properties

The photophysical properties of S-TPA-PI and S-2TPA-2PI were first explored in dimethyl sulfoxide (DMSO) and aqueous solution. The UV-vis absorption and fluorescence spectra of isolated molecules (in DMSO) are presented in Fig. 2a. S-TPA-PI and S-2TPA-2PI showed similar absorption and emission spectra, with the maximum absorption peak (λ_{abs}) of ~450 nm and the maximum emission peak (λ_{em}) of ~744 nm, resulting from the homologous chromophore. The differences in optical properties appeared when molecules were in an aqueous solution (Fig. 2b). The absorption of S-2TPA-2PI was about 463 nm, which was bathochromically shifted by ~7 nm compared with monomeric S-TPA-PI.

Likewise, the emission peak of S-2TPA-2PI also red-shifted by ~11 nm, reaching around 646 nm, which might contribute to the different aggregation patterns in the aqueous solution. The luminescence of both S-TPA-PI and S-2TPA-2PI was significantly enhanced with an increasing water fraction (f_w), presenting pronounced AIE characters (Fig. 2c), which further implied that

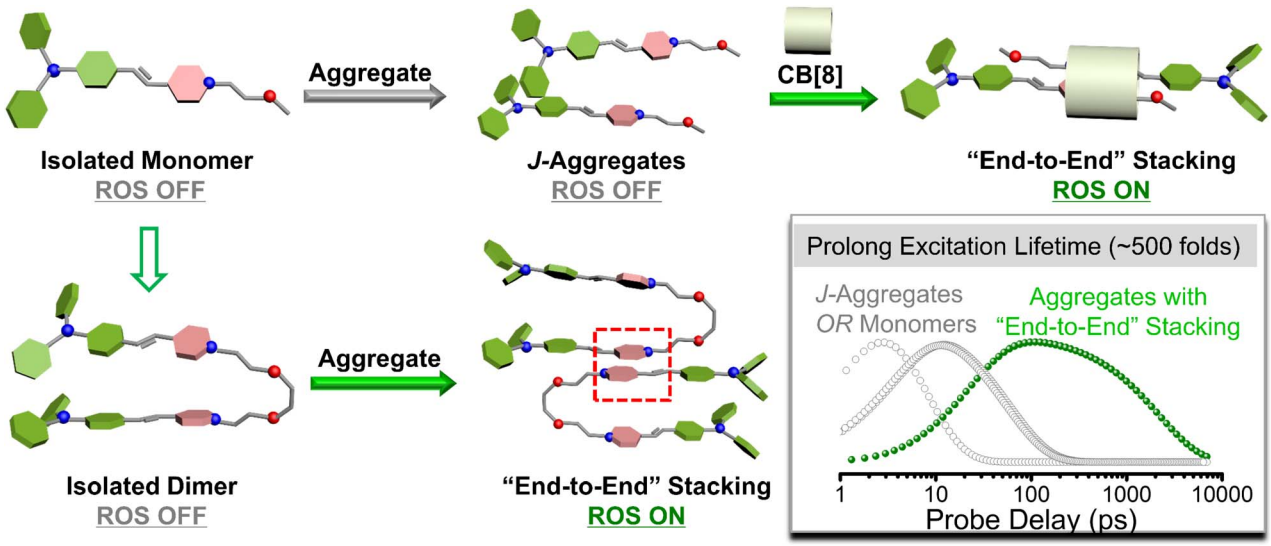

Scheme 1 Schematic illustration of dimer engineering.

© 2023 The Author(s). Published by the Royal Society of Chemistry

Open Access Article. Published on 12 December 2022. Downloaded on 12/5/2025 11:51:35 PM.
This article is licensed under a Creative Commons Attribution-NonCommercial 3.0 Unported Licence.

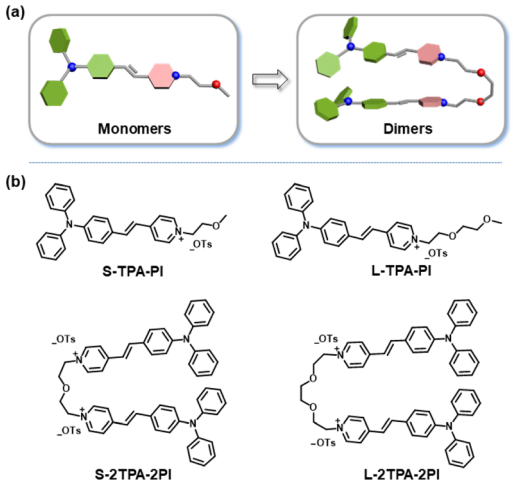

Fig. 1 (a) The molecular model and (b) structure details of monomers (S-TPA-PI and L-TPA-PI) and dimers (S-2TPA-2PI and L-2TPA-2PI).

both the molecules had good planarity and rigidity upon aggregation.[35,36] Remarkably, the fluorescence quantum yield of dimeric S-2TPA-2PI in water was only 1.85%, much lower than 14.27% of S-TPA-PI, indicating the presence of additional non-radiative transition channels for aggregates of the dimer. Particle sizes in AIE were measured through dynamic light scattering (DLS). As shown in Fig. 2d and S13,† the nanoparticles with an average size of <100 nm were formed in an aqueous solution other than DMSO, which was consistent with the data from transmission emission microscopy (TEM) (S14†). At the same time, a similar phenomenon could be observed for L-TPA-PI and L-2TPA-2PI with long-chain molecules (Fig. S15–17†).

Photogenerated ROS

Generally, ROS could be produced in two pathways, one by energy transfer (type II) to generate singlet oxygen ($^1O_2$), and the other by electron transfer (type I) to produce free radicals (such as $^{\bullet}OH$, $O_2^{-\bullet}$)[37,38] which were monitored by using various fluorescence indicators or an electron spin resonance (ESR) spectrometer. First, type I and II ROS species were determined by using an ESR spectrometer with free radical indicator 5, 5-dimethyl-1-pyrroline-*N*-oxide (DMPO) for $O_2^{-\bullet}$ and 2, 2, 6, 6-tetramethyl-1-piperidinyloxy (TEMPO) for $^1O_2$ (Fig. 2e and S18†).[39] Upon irradiation using an LED lamp, the more intensive signals of $O_2^{-\bullet}$ and $^1O_2$ were successfully captured in the aggregate of S-2TPA-2PI rather than that of S-TPA-PI, showing that S-TPA-PI and S-2TPA-2PI had different oxygen free radical releasing capacities *via* the type I or II pathway.[40] Moreover, type II ROS generations of S-TPA-PI and S-2TPA-2PI in isolated states and aggregates were investigated, wherein 9, 10-anthracenediyl-bis-(methylene)-dimalonic acid (ABDA) was utilized as the $^1O_2$ indicator.[41] $^1O_2$ could cause continuous oxidation of ABDA, resulting in the decreasing absorbance of ABDA. As exhibited in Fig. 2f and S19,† upon irradiation using an LED lamp, the absorption of ABDA rapidly dropped only with S-2TPA-2PI-aggregates, while a negligible decline in absorption was detected for S-2TPA-2PI in the isolated state. The $^1O_2$ generation abilities of S-TPA-PI were particularly weak whether in DMSO or aqueous solutions.

Besides, the yields of $^1O_2$ (Φ) in an aqueous solution were calculated using RB as a reference as shown in Fig. S20†. In the state of aggregation, S-2TPA-2PI showed a Φ value more than 20 times that of S-TPA-PI. Similarly, the aggregation-induced generation of $^1O_2$ was also observed in dimeric L-2TPA-2PI with a long-chain-linker (Fig. S21†) even at low concentrations

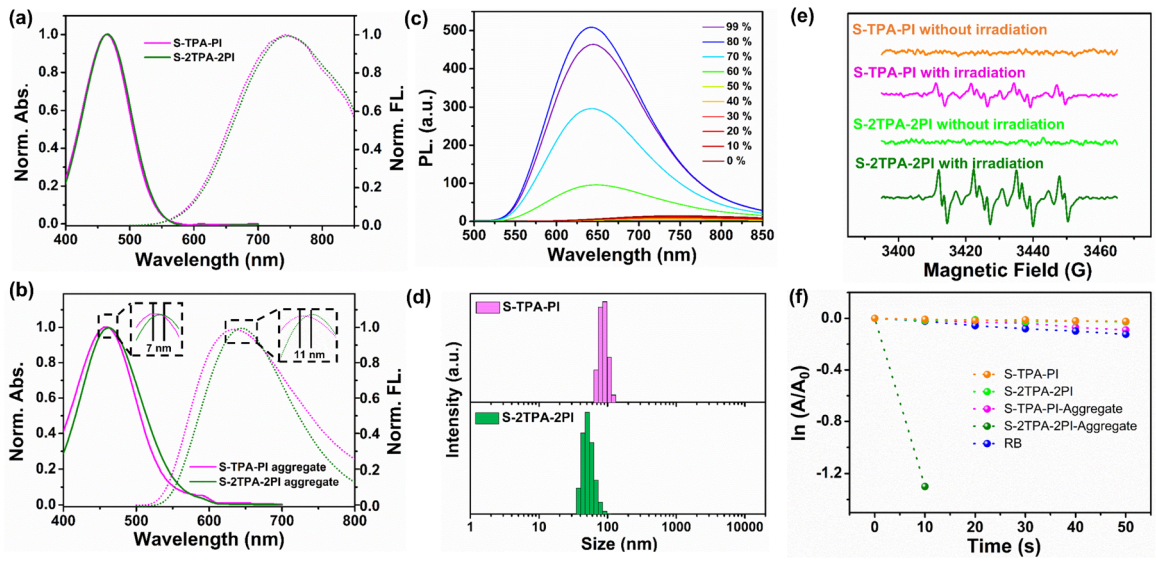

Fig. 2 The normalized absorbance and fluorescence spectra of S-TPA-PI (pink line) and S-2TPA-2PI (green line) in (a) DMSO or (b) aqueous solution; (c) the AIE spectra of S-2TPA-2PI with different water fractions (f_w: 0–99%); (d) size distribution of S-TPA-PI and S-2TPA-2PI confirmed by DLS in aqueous solution; (e) the electron spin resonance spectra of DMPO/S-TPA-PI and DMPO/S-2TPA-2PI under LED lamp irradiation (50 mW cm^{-2}) for 0 or 2 min; (f) the ability of degradation toward ABDA with PSs (10 μM) in DMSO (10 μM) or in H_2O (1% DMSO) under LED lamp irradiation (50 mW cm^{-2}).

Open Access Article. Published on 12 December 2022. Downloaded on 12/5/2025 11:51:35 PM. This article is licensed under a Creative Commons Attribution-NonCommercial 3.0 Unported Licence.

(Fig. S22 and 23†), which further manifested that S-2TPA-2PI and L-2TPA-2PI have the potential for low dose PDT.[42]

The mechanism of photogenerated ROS

To study the mechanism of ROS generation, the single crystals for S-TPA-PI and S-2TPA-2PI were obtained by evaporating ethanol, which was crystallized in the triclinic crystal system with the $\bar{P}1$ space group. Further crystallographic details are given in Table S1 and S2 (ESI†). S-TPA-PI displayed decent planarity, wherein the dihedral angle between the pyridine segment and TPA segment was 15.03° or 25.55° (two molecules in the crystal cell) (Fig. 3a).

The adjacent S-TPA-PI showed staggered stacking due to the propeller TPA with a π–π distance of ~3.69 Å, demonstrating the *J*-aggregates that favor fluorescence emission[43] (Fig. 3b and c). In sharp contrast, two chromophores in dimeric S-2TPA-2PI presented different planarities with dihedral angles of 41.44° and 10.23° as shown in Fig. 3d, possibly attributed to the limitation of the oligo-ethylene glycol linker. Interestingly, compared with *J*-aggregation in S-TPA-PI, both the chromophores in S-2TPA-2PI formed "end-to-end" stacking with a π–π distance of ~3.29 Å and 3.34 Å (Fig. 3e and f). In general, monomeric S-TPA-PI and dimeric S-2TPA-2PI exhibited different aggregation patterns that may be the key to the "ROS OFF/ON".

To further validate the above conclusion, an exploratory experiment was designed to change the stacking pattern of S-TPA-PI with cucurbit[8]uril (CB[8]), which could hold two pyridinium salts through host–guest interaction, formatting "end-to-end" stacking.[44] As depicted in Fig. 3g, S-TPA-PI aggregates alone cannot generate ROS under white-light irradiation. However, when CB[8] was employed, signals of singlet oxygen were observed as shown in Fig. 3h, demonstrating the huge effect of modulating stacking patterns on photo-generated ROS.

To gain insight into the divergence of photophysical processes resulting from different aggregation patterns, time-dependent density functional theory (TD-DFT) calculations were performed with the geometry of the isolated state, *J*-aggregates, and "end-to-end" stacking aggregates. As seen in Fig. 4g, ΔE_{ST} is 0.925 eV (isolated state), 0.487 eV (*J*-aggregates), and 0.386 eV ("end-to-end" stacking aggregates), demonstrating that "end-to-end" stacking could reduce the energy difference between S_1 and T_1. Moreover, the SOC strength ($S_1|\bar{H}_{SOC}|T_1$) was calculated to be 0.24 cm^{-1} (isolated state), 0.14 cm^{-1} (*J*-aggregates), and 0.25 cm^{-1} ("end-to-end" stacking aggregates), respectively. The "end-to-end" stacking aggregates showed an

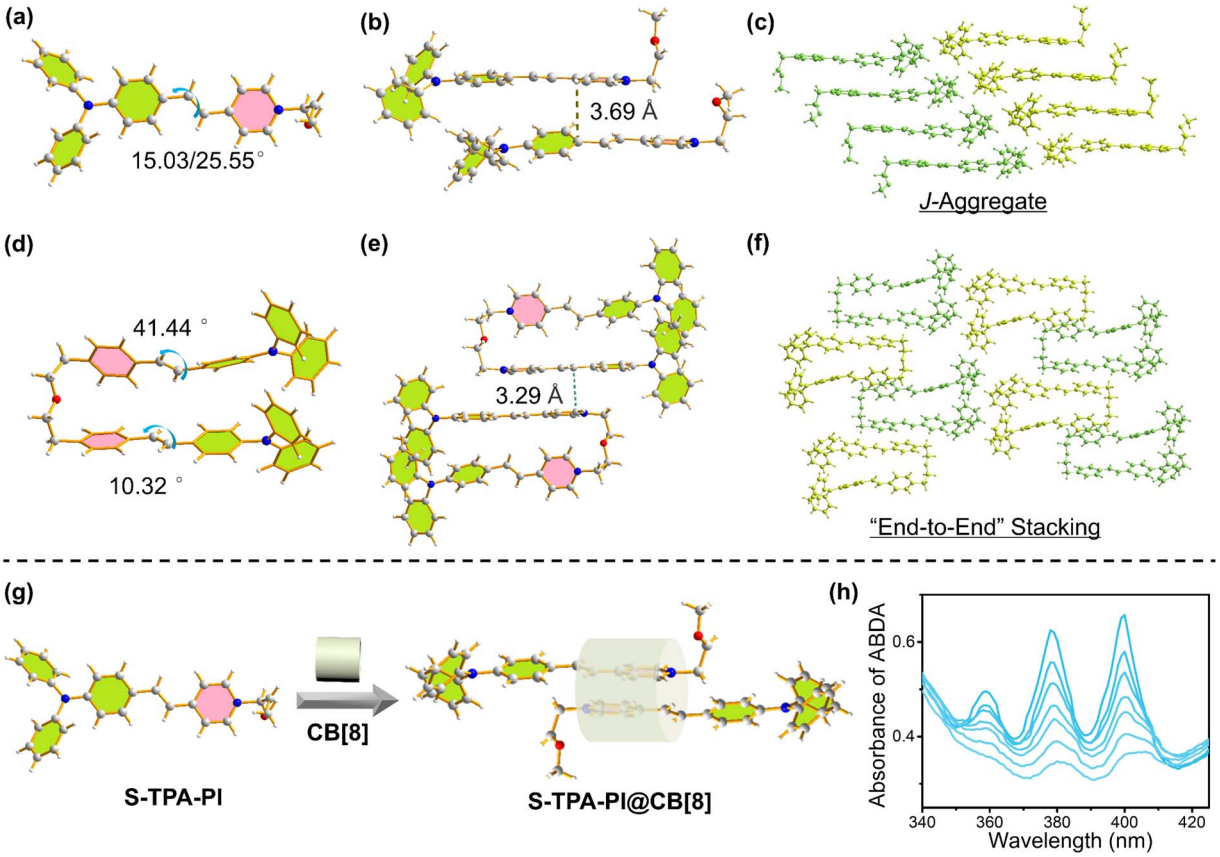

Fig. 3 Single crystal structures for (a) S-TPA-PI and (d) S-2TPA-2PI; structural characterization of intermolecular geometry for (b) S-TPA-PI and (e) S-2TPA-2PI; Molecular stacking of (c) S-TPA-PI and (f) S-2TPA-2PI; (g) the self-assembly diagram of S-TPA-PI@CB[8]; (h) the decomposition curves of ABDA in the presence of S-TPA-PI@CB[8] under LED lamp irradiation (50 mW cm^{-2}).

© 2023 The Author(s). Published by the Royal Society of Chemistry

Open Access Article. Published on 12 December 2022. Downloaded on 12/5/2025 11:51:35 PM.
This article is licensed under a Creative Commons Attribution-NonCommercial 3.0 Unported Licence.

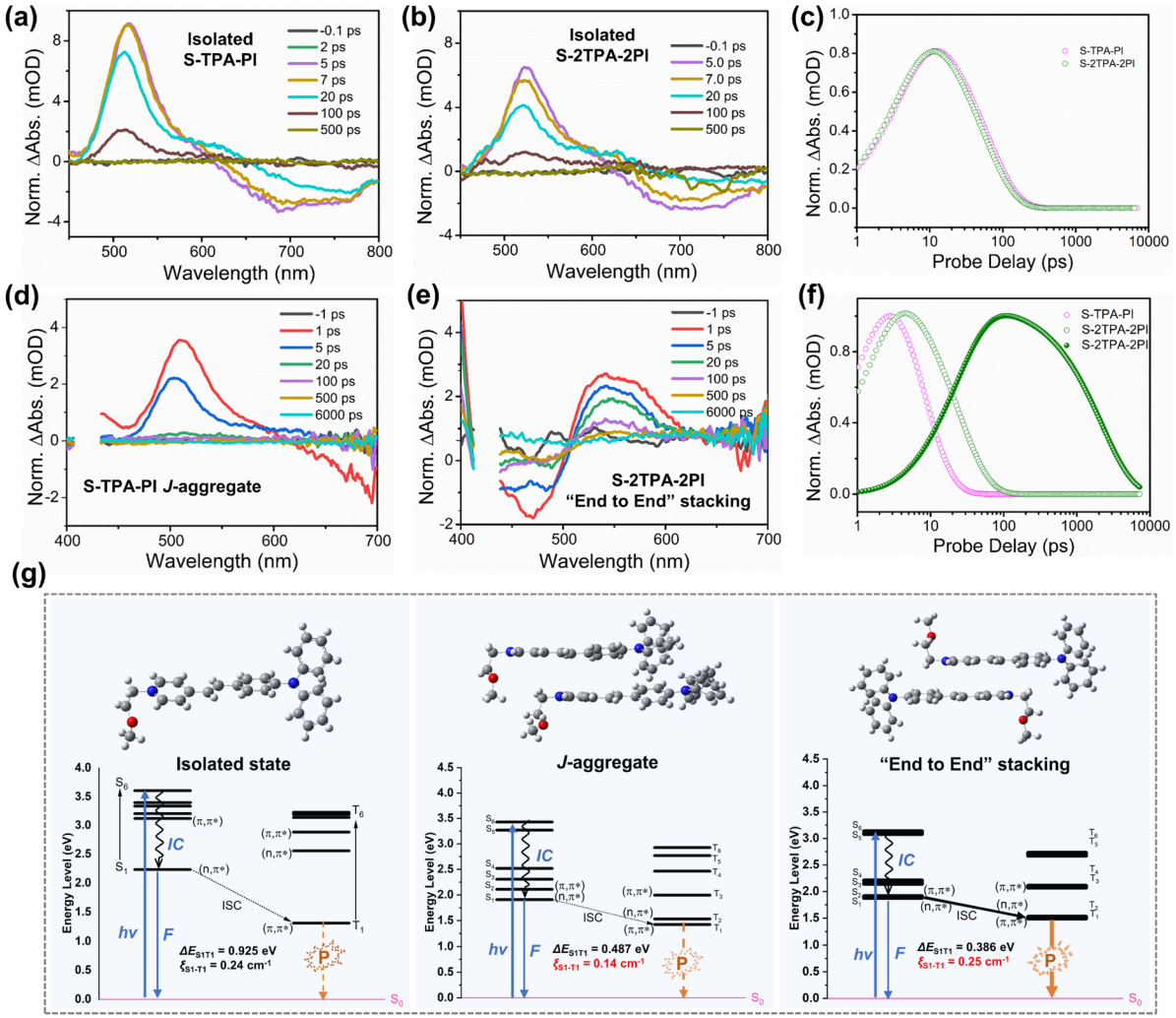

Fig. 4 The analysis of transient absorption spectra of (a) S-TPA-PI and (b) S-2TPA-2PI in DMSO; (c) the dynamics corresponding to (a and b) for excited state absorption of isolated S-TPA-PI and S-2TPA-2PI, respective the analysis of transient absorption spectra of (d) S-TPA the and (e) S-2TPA-2PI in the H_2O; (f) the dynamics corresponding to (d and e) for excited state absorption of aggregated S-TPA-PI and S-2TPA-2PI. (g) The energy level diagrams of the isolated state, *J*-aggregate, and "end-to-end" stacking adopted from single crystal data based on the M06-2X functional and RI/J approximation calculations in the gas phase.

enhanced ISC rate constant (k_{ISC}) for both the lowest ΔE_{ST} and highest SOC, which could benefit the formation of an excited triplet state for ROS generation. Moreover, excited-state dynamics of two molecules in DMSO or aqueous solution were investigated in an argon atmosphere by femtosecond (fs) transient absorption (TA) spectroscopy. In DMSO, the excited-state absorption (ESA) peaks of monomers and dimers were both at ~530 nm. The TA spectra of the four molecules displayed a fast dynamic decay with a time constant of a few picoseconds.

And their decay dynamics were well fit by using a single exponential function with similar exciton lifetimes of 58.9 ps (S-TPA-PI), 53.6 ps (S-2TPA-2PI), 62.7 ps (L-TPA-PI), and 57.5 ps (L-2TPA-2PI), resulting from homologous molecules with the same chromophore (Fig. 4a–c, S24, and 25†). However, the difference in exciton lifetime was observed in aqueous solutions. The ESA peaks for the monomers were at ~525 nm, which fast decayed with the exciton lifetimes of 7.3 ps (S-TPA-PI) and 7.8 ps (L-TPA-PI) (Fig. 4d and S26†). Surprisingly, dimers exhibited ESA peaks at ~550 nm, which showed both a slightly longer lifetime (25–40 ps) and a much longer lifetime (1.7–4.3 ns) as shown in Fig. 4e, f, and S26†. Such an exponential growth of exciton lifetimes in aggregates of the dimer can be attributed to the distinctive "end-to-end" stacking, which provided sufficient time to ensure subsequent processes.[45] To further prove this conjecture, the excited-state dynamics of S-TPA-PI@CB[8] were explored in an aqueous solution and showed a longer lifetime (~10 ns) (Fig. S27†), which manifested that the "end-to-end" stacking was particularly beneficial to increase the exciton lifetimes and promote ROS generation. Moreover, the lifetime of S-2TPA-2PI in an air atmosphere was calculated to be 2.20 ns (Fig. S28†), which was shorter than 3.87 ns in an argon atmosphere, offering valid evidence of an effective electron-transfer process between oxygen and S-2TPA-2PI-aggregates.

© 2023 The Author(s). Published by the Royal Society of Chemistry

Open Access Article. Published on 12 December 2022. Downloaded on 12/5/2025 11:51:35 PM. This article is licensed under a Creative Commons Attribution-NonCommercial 3.0 Unported Licence.

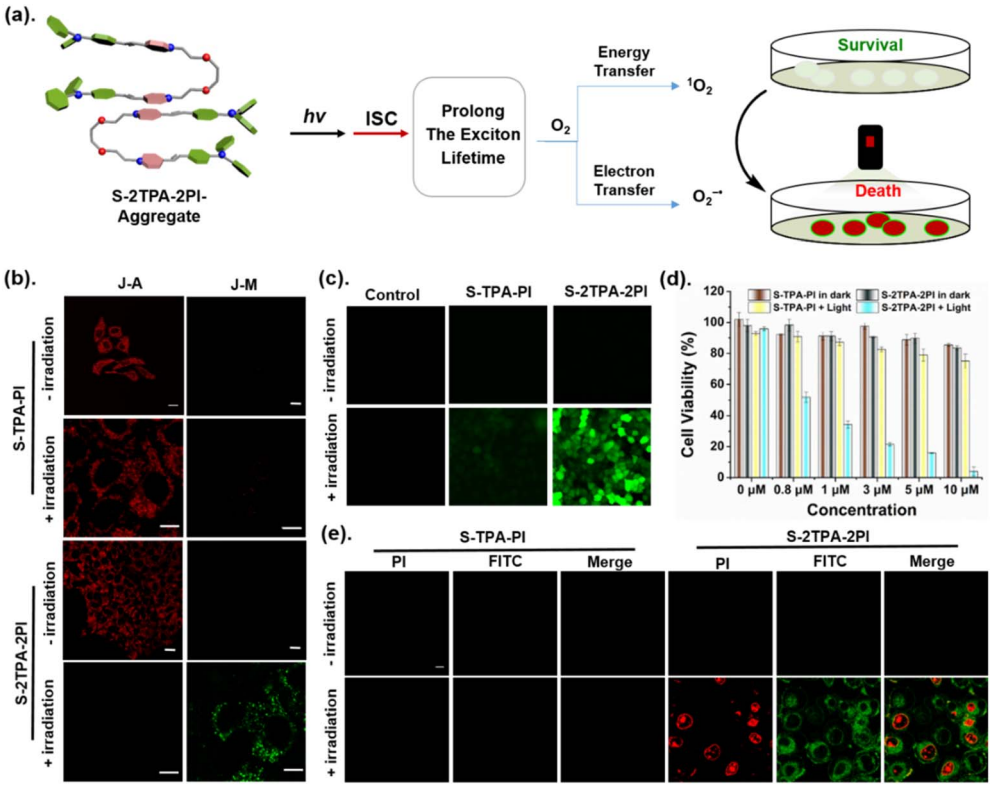

Fig. 5 (a) The schematic diagram of photogeneration of ROS and the suppressing effect on the cancer cell; (b) confocal images of HepG2 cells separately treated with S-2TPA-2PI or S-2TPA-2PI, followed by white light irradiation (400–700 nm, 50 mW cm^{-2}) for 10 min and then incubated with JC-10 for 15 min and (c) DCFH-DA for 20 min; (d) the viabilities of HepG2 cells incubated with S-2TPA-2PI or S-2TPA-2PI at various concentrations without or with LED lamp irradiation for 10 min; (e). PI (2 μM) and FITC (5 μM) for 12 min (red channel: λ_{ex} = 543 nm and λ_{em} = 600–660 nm and green channel: λ_{ex} = 488 nm and λ_{em} = 500–560 nm). Scale bar: 20 μm.

To sum up, aggregates with "end-to-end" stacking showed both an enhanced k_{isc} and prolonged exciton lifetime, promoting the ISC process, thus causing efficient ROS generation upon illumination. Theoretically, such aggregates should be more likely to generate phosphoresce in an oxygen-free and low-temperature environment due to the efficient ISC. Therefore, the temperature-dependent phosphorescence spectra are supplemented in Fig. S29.† Indeed, compared with S-TPA-PI, its dimer (S-2TPA-2PI) displayed a phosphorescence peak at around 720 nm with a longer phosphorescence lifetime (2.69 μs) at 135 K, indicating that the triplet excited state could be formed in S-2TPA-2PI rather than S-TPA-PI. These results further confirmed that the efficient generation of ROS by S-2TPA-2PI aggregates with "end-to-end" stacking could be attributed to the elevated ISC process. The corresponding excited state processes of ROS generation of different aggregation patterns are outlined in the schematic diagram in Fig. S30.†

Due to the existence of the type I process which involves electron transfer, photocurrent and charge transfer resistance (R_{ct}) were measured as shown in Fig. S31,† revealing the significantly enhanced photocurrent in the dimeric S-2TPA-2PI-aggregate, which possibly resulted from the stable exciton in S-2TPA-2PI with "end-to-end" stacking, enhancing type I ROS. Meanwhile, the photo-stability and recyclability were satisfactory, which may benefit further biological applications.

Photo-induced mitophagy and cancer cell apoptosis

Considering that ROS generation was induced by "end-to-end" stacking, the application in cells has been further explored. First, S-2TPA-2PI or S-TPA-PI at a concentration of 0.6 μM were added to HepG2 cells with 30 min of incubation. Fig. S32a and b† show that S-2TPA-2PI and S-TPA-PI were anchored on mitochondria in the dark and further verified with splendid overlap *via* green emission of Mito-Tracker Green.[46] Upon LED lamp (50 mW cm^{-2}) irradiation, S-TPA-PI was still anchored on mitochondria with a high Pearson's correlation coefficient of 0.78, while the filamentous mitochondria of HepG2 cells cultured with S-2TPA-2PI were gradually fractured and autophagic vacuoles emerged, possibly due to the mitophagy induced by ROS. Simultaneously, the co-localization experiments showed that the yellow emission of S-2TPA-2PI was well overlapped with the cyan emission of MDC (a commercial dye for autophagic vacuoles),[47] further implying that mitophagy took place with irradiation. In order to observe the microstructure of mitochondria and autophagy vacuoles, Ariyscan laser scanning microscopy was carried out in Fig. 32c.† The subtle mitochondrial frames with ridges were monitored on the cell incubated with S-2TPA-2PI in the dark. However, the

© 2023 The Author(s). Published by the Royal Society of Chemistry

Open Access Article. Published on 12 December 2022. Downloaded on 12/5/2025 11:51:35 PM.
This article is licensed under a Creative Commons Attribution-NonCommercial 3.0 Unported Licence.

autophagosome with a vesicular structure appeared upon the white light, which adequately illustrated that self-releasing ROS of S-2TPA-2PI could induce mitochondrial autophagy with the emergence of autophagic vacuoles.[48]

Such an excellent ROS production capability of S-2TPA-2PI motivated us to investigate the effect on cancer cell inhibition (Fig. 5a). At first, dichlorofluorescein diacetate (DCFH-DA) was used for determining ROS generation *in vivo*. As displayed in Fig. 5c, HepG2 cells cultured with S-2TPA-2PI (0.6 μM) showed a more remarkable green fluorescence compared to S-TPA-PI (0.6 μM) after irradiating with an LED lamp for 5 min. This result testified that S-2TPA-2PI-treated cells could generate ROS compared to S-TPA-PI-treated cells. Considering the aggregation-induced generation of ROS (AIG-ROS) and excellent mitochondrial targeting ability of S-2TPA-2PI, the mitochondrial membrane potential (MMP) was measured by using a sensitive probe (JC-10). As shown in Fig. 5b, S-TPA-PI cultured cells still showed red signals before and after irradiation, while S-2TPA-2PI showed green fluorescence after irradiation. The results further revealed that S-2TPA-2PI generating ROS aroused MMP collapse and mitochondrial autophagy under irradiation. After that, the photodynamic cell suppression efficiency of S-TPA-PI and S-2TPA-2PI was tested through MTT (3-(4, 5-dimethylthiazol-2-yl)-2, 5-diphenyltetrazolium bromide) assay. In the dark, S-TPA-PI and S-2TPA-2PI showed negligible cytotoxicity and optimal biocompatibility (Fig. 5d). While the cells incubated by using S-2TPA-2PI were irradiated with an LED lamp for 10 min, the cell survival rate decreased to varying degrees. The light cytotoxicity of S-2TPA-2PI was significantly better than that of S-TPA-PI at the same dose. Meanwhile, the cancer cell suppression abilities of S-TPA-PI and S-2TPA-2PI were further evaluated through cell fluorescence imaging. As observed in Fig. 5e, viable apoptotic cells (green) and late apoptotic ones (red) were differentiated by using Annexin V-FITC (FITC) and propidium iodide (PI), respectively. In the dark, both the green and red channel hardly showed fluorescence in HepG2 cells with 3 μM PS incubation. Upon LED lamp irradiation, green fluorescence obviously emerged and adhered to the cell membrane, and red fluorescence obviously appeared and was anchored to the nucleus. These results were consistent with the results of MTT assay, reaffirming the excellent photo-cytotoxicity of S-2TPA-2PI in aggregation.

Conclusions

This study reported the effect of the aggregation pattern on ROS release through the construction of organic PSs with homologous chromophores. Dimeric S-2TPA-2PI exhibited an upsurge of photogenerated ROS compared to monomeric S-TPA-PI, attributed to the unique "end-to-end" stacking, which could prolong the exciton lifetime by 500–1000 fold and enhance the ISC rate constant. Furthermore, cucurbit[8]uril was employed to tune the stacking pattern of monomeric S-TPA-PI through host–guest interactions, achieving ROS enhancement under light, validating the promotion of photogenerated ROS by "end-to-end" stacking. Additionally, S-2TPA-2PI with mitochondrial targeting ability could lead to rapid mitophagy for significant cancer cell suppression for PDT. This work will not only provide insights into the area of organic aggregate related ISC but also benefit the development of PSs.

Data availability

All the data supporting this article have been included in the main text and the ESI.†

Author contributions

Junjun Wang: conceptual design, investigation, synthesis of compounds, processing of test data, writing-original draft. Hao Li: the processing of data on femtosecond (fs) transient absorption (TA) spectroscopy. Yicai Zhu, Mingdi Yang, and Jing Huang: processing of test data. Xiaojiao Zhu and Zhou Lu: funding acquisition, validation. Zhipeng Yu and Hongping Zhou: method inquiry, project administration, funding acquisition, writing-review, and editing.

Conflicts of interest

There are no conflicts to declare.

Acknowledgements

This work was supported by the National Natural Science Foundation of China (51972001 and 22005002), Natural Science Fund of the Education Department of Anhui province (KJ2019A0013). Changjiang Scholars and Innovative Research Team in University, and Anhui University Scientific Research Start-up Fund (S020118002/039 and S020318006/005). The authors acknowledge the support of the Key Lab of Photovoltaic and Energy Conservation Materials, Chinese Academy of Sciences (PECL2019KF012) and the Anhui Provincial Natural Science Foundation (2008085MB43). We would like to acknowledge the Imaging Unit at the Core Facility Centre for Life Science, University of Science and Technology of China and the research staff (Zhenbang Liu, M.S.) who contributed valuable technical expertise and assistance to this project.

References

1 X. Wu, M. Yang, J. S. Kim, R. Wang, G. Kim, J. Ha, H. Kim, Y. Cho, K. T. Nam and J. Yoon, *Angew. Chem., Int. Ed.*, 2022, **61**, e202200808.
2 L. Gourdon, K. Cariou and G. Gasser, *Chem. Soc. Rev.*, 2022, **51**, 1167–1195.
3 Y. Lee and D.-H. Kim, *Nat. Biomed. Eng.*, 2019, **3**, 5–6.
4 H. Lee, Y. Lee, C. Song, H. R. Cho, R. Ghaffari, T. K. Choi, K. H. Kim, Y. B. Lee, D. Ling, H. Lee, S. J. Yu, S. H. Choi, T. Hyeon and D.-H. Kim, *Nat. Commun.*, 2015, **6**, 10059.
5 J. Zhang, Q. Jia, Z. Yue, J. Huo, J. Chai, L. Yu, R. Nie, H. Shao, Y. Zhao, P. Li and W. Huang, *Adv. Mater.*, 2022, **34**, 2200334.
6 B. Tang, W. Xu, J.-F. Xu and X. Zhang, *Angew. Chem., Int. Ed.*, 2021, **60**, 9384–9388.

Open Access Article. Published on 12 December 2022. Downloaded on 12/5/2025 11:51:35 PM. This article is licensed under a Creative Commons Attribution-NonCommercial 3.0 Unported Licence.

7 J. Guo, C. Yang and Y. Zhao, *Acc. Chem. Res.*, 2022, **55**, 1160–1170.
8 K. Li, Y. Chen, J. Wang and C. Yang, *Coord. Chem. Rev.*, 2021, **433**, 213755.
9 Z. Wang, L. Huang, Y. Yan, A. M. El-Zohry, A. Toffoletti, J. Zhao, A. Barbon, B. Dick, O. F. Mohammed and G. Han, *Angew. Chem., Int. Ed.*, 2020, **59**, 16114–16121.
10 Z. Xu, Y. Jiang, Y. Shen, L. Tang, Z. Hu, G. Lin, W.-C. Law, M. Ma, B. Dong, K.-T. Yong, G. Xu, Y. Tao, R. Chen and C. Yang, *Mater. Horiz.*, 2022, **9**, 1283–1292.
11 Y.-F. Xiao, W.-C. Chen, J.-X. Chen, G. Lu, S. Tian, X. Cui, Z. Zhang, H. Chen, Y. Wan, S. Li and C.-S. Lee, *ACS Appl. Mater. Interfaces*, 2022, **14**, 5112–5121.
12 B. Gu, W. Wu, G. Xu, G. Feng, F. Yin, P. H. J. Chong, J. Qu, K.-T. Yong and B. Liu, *Adv. Mater.*, 2017, **29**, 1701076.
13 S. Gan, W. Wu, G. Feng, Z. Wang, B. Liu and B. Z. Tang, *Small*, 2022, **18**, 2202242.
14 Y. Yu, S. Wu, L. Zhang, S. Xu, C. Dai, S. Gan, G. Xie, G. Feng and B. Z. Tang, *Biomaterials*, 2022, **280**, 121255.
15 T. Zhang, Z. Liu, W. Tang, D. Zhu, M. Lyu, J. W. Y. Lam, Q. Huang and B. Z. Tang, *Nano Today*, 2022, **46**, 101620.
16 R. Xu, W. Chi, Y. Zhao, Y. Tang, X. Jing, Z. Wang, Y. Zhou, Q. Shen, J. Zhang, Z. Yang, D. Dang and L. Meng, *ACS Nano*, 2022, DOI: **10.1021/acsnano.2c04465**.
17 Z. Liu, H. Zou, Z. Zhao, P. Zhang, G.-G. Shan, R. T. K. Kwok, J. W. Y. Lam, L. Zheng and B. Z. Tang, *ACS Nano*, 2019, **13**, 11283–11293.
18 O. J. Dautel, G. Wantz, R. Almairac, D. Flot, L. Hirsch, J.-P. Lere-Porte, J.-P. Parneix, F. Serein-Spirau, L. Vignau and J. J. E. Moreau, *J. Am. Chem. Soc.*, 2006, **128**, 4892–4901.
19 N. J. Hestand and F. C. Spano, *Acc. Chem. Res.*, 2017, **50**, 341–350.
20 F. C.-M. Leung, S. Y.-L. Leung, C. Y.-S. Chung and V. W.-W. Yam, *J. Am. Chem. Soc.*, 2016, **138**, 2989–2992.
21 J. Wang, D. Liu, Y. Zhu, S. Zhou and S. Guan, *Appl. Catal., B*, 2018, **231**, 251–261.
22 Z. Wen, T. Yang, D. Zhang, Z. Wang, S. Dong, H. Xu, Y. Miao, B. Zhao and H. Wang, *J. Mater. Chem. C*, 2022, **10**, 3396–3403.
23 Y.-F. Kang, W.-K. Chen, K.-X. Teng, L.-Y. Wang, X.-C. Xu, L.-Y. Niu, G. Cui and Q.-Z. Yang, *CCS Chem.*, 2021, 1–13.
24 C. Ji, Q. Gao, X. Dong, W. Yin, Z. Gu, Z. Gan, Y. Zhao and M. Yin, *Angew. Chem., Int. Ed.*, 2018, **57**, 11384–11388.
25 C. Ji, L. Lai, P. Li, Z. Wu, W. Cheng and M. Yin, *Aggregate*, 2021, **2**, e39.
26 T. Lai, L. Xiao, K. Deng, T. Liang, X. Chen, X. Peng and Y. Cao, *ACS Appl. Mater. Interfaces*, 2018, **10**, 668–675.
27 E. Sebastian and M. Hariharan, *J. Am. Chem. Soc.*, 2021, **143**, 13769–13781.
28 A. Aster, F. Zinna, C. Rumble, J. Lacour and E. Vauthey, *J. Am. Chem. Soc.*, 2021, **143**, 2361–2371.
29 J. Zhang, H. Sakai, K. Suzuki, T. Hasobe, N. V. Tkachenko, I. Y. Chang, K. Hyeon-Deuk, H. Kaji, T. Teranishi and M. Sakamoto, *J. Am. Chem. Soc.*, 2021, **143**, 17388–17394.
30 C. M. Mauck, P. E. Hartnett, E. A. Margulies, L. Ma, C. E. Miller, G. C. Schatz, T. J. Marks and M. R. Wasielewski, *J. Am. Chem. Soc.*, 2016, **138**, 11749–11761.
31 S. Zeena and K. G. Thomas, *J. Am. Chem. Soc.*, 2001, **123**, 7859–7865.
32 Y. Bu, T. Xu, X. Zhu, J. Zhang, L. Wang, Z. Yu, J. Yu, A. Wang, Y. Tian, H. Zhou and Y. Xie, *Chem. Sci.*, 2020, **11**, 10279–10286.
33 J. Wang, X. Zhu, J. Zhang, H. Wang, G. Liu, Y. Bu, J. Yu, Y. Tian and H. Zhou, *ACS Appl. Mater. Interfaces*, 2020, **12**, 1988–1996.
34 X. Zhu, G. Liu, Y. Bu, J. Zhang, L. Wang, Y. Tian, J. Yu, Z. Wu and H. Zhou, *Anal. Chem.*, 2020, **92**, 10815–10821.
35 M. Wu, X. Liu, H. Chen, Y. Duan, J. Liu, Y. Pan and B. Liu, *Angew. Chem., Int. Ed.*, 2021, **60**, 9093–9098.
36 B. Situ, S. Chen, E. Zhao, C. W. T. Leung, Y. Chen, Y. Hong, J. W. Y. Lam, Z. Wen, W. Liu, W. Zhang, L. Zheng and B. Z. Tang, *Adv. Funct. Mater.*, 2016, **26**, 7132–7138.
37 D. Duosiken, R. Yang, Y. Dai, Z. Marfavi, Q. Lv, H. Li, K. Sun and K. Tao, *J. Am. Chem. Soc.*, 2022, **144**, 2455–2459.
38 C. Mu, W. Wang, J. Wang, C. Gong, D. Zhang and X. Zhang, *Angew. Chem., Int. Ed.*, 2020, **59**, 21515–21519.
39 J. G. Roberts, M. A. Voinov, A. C. Schmidt, T. I. Smirnova and L. A. Sombers, *J. Am. Chem. Soc.*, 2016, **138**, 2516–2519.
40 D. Chen, Q. Yu, X. Huang, H. Dai, T. Luo, J. Shao, P. Chen, J. Chen, W. Huang and X. Dong, *Small*, 2020, **16**, 2001059.
41 Y. Wang, S. Xu, L. Shi, C. Teh, G. Qi and B. Liu, *Angew. Chem., Int. Ed.*, 2021, **60**, 14945–14953.
42 Y. Liu, Y. Xu, Z. Zhang, Y. Huo, D. Chen, W. Ma, K. Sun, G. Y. Tonga, G. Zhou, D. S. Kohane and K. Tao, *Nano Lett.*, 2019, **19**, 5515–5523.
43 M. Li, W. Sun, R. Tian, J. Cao, Y. Tian, B. Gurram, J. Fan and X. Peng, *Biomaterials*, 2021, **269**, 120532.
44 H.-J. Yu, Q. Zhou, X. Dai, F.-F. Shen, Y.-M. Zhang, X. Xu and Y. Liu, *J. Am. Chem. Soc.*, 2021, **143**, 13887–13894.
45 S. Liu, G. Feng, B. Z. Tang and B. Liu, *Chem. Sci.*, 2021, **12**, 6488–6506.
46 G. Li, Q. Lin, L. Sun, C. Feng, P. Zhang, B. Yu, Y. Chen, Y. Wen, H. Wang, L. Ji and H. Chao, *Biomaterials*, 2015, **53**, 285–295.
47 N. Mizushima, *Int. J. Biochem. Cell Biol.*, 2004, **36**, 2491–2502.
48 S. Kissing, S. Rudnik, M. Damme, R. Lüllmann-Rauch, A. Ichihara, U. Kornak, E.-L. Eskelinen, S. Jabs, J. Heeren, J. K. De Brabander, A. Haas and P. Saftig, *Autophagy*, 2017, **13**, 670–685.

© 2023 The Author(s). Published by the Royal Society of Chemistry